Automating Model Generation For Image Based Cardiac Flow Simulation

Fanwei Kong
Mechanical Engineering Department,
University of California, Berkeley,
Berkeley, CA 94709
e-mail: fanwei_kong@berkeley.edu

Shawn C. Shadden
Mechanical Engineering Department,
University of California, Berkeley,
Berkeley, CA 94709
e-mail: shadden@berkeley.edu

ABSTRACT

Computational fluid dynamics (CFD) modeling of left ventricle (LV) flow combined with patient medical imaging data has shown great potential in obtaining patient-specific hemodynamics information for functional assessment of the heart. A typical model construction pipeline usually starts with segmentation of the LV by manual delineation followed by mesh generation and registration techniques using separate software tools. However, such approaches usually require significant time and human efforts in the model generation process, limiting large-scale analysis. In this study, we propose an approach towards fully automating the model generation process for CFD simulation of LV flow to significantly reduce LV CFD model generation time. Our modeling framework leverages a novel combination of techniques including deep-learning based segmentation, geometry processing, and image registration to reliably reconstruct CFD-suitable LV models with little-to-no user intervention. We utilized an ensemble of 2D convolutional neural networks (CNNs) for automatic segmentation of cardiac structures from 3D patient images and our segmentation approach outperformed recent state-of-the-art segmentation techniques when evaluated on benchmark data containing both MR and CT cardiac scans. We demonstrate that through a combination of segmentation and geometry processing, we were able to robustly create CFD-suitable LV meshes from segmentations for 78 out of 80 test cases. Although the focus on this study is on image-to-mesh

generation, we demonstrate the feasibility of this framework in supporting LV hemodynamics modeling by performing CFD simulations from two representative time-resolved patient-specific image data sets.

NOMENCLATURE

CFD Computational fluid dynamics

MR Magnetic resonance

CT Computed tomography

b-SSFP balanced steady state free precession

MMWHS Multi-Modality Whole Heart Segmentation

LV Left ventricle

LA Left atrium

RA Right atrium

RV Right ventricle

AO Aortic opening

MO Mitral opening

CNN Convolutional neural network

INTRODUCTION

Image-based modeling of blood flow is an important research area in biomedical engineering. It is based on applying computational fluid dynamics (CFD) to image-based computer models of the heart, arteries or veins in order to compute patient-specific blood flow information that is not measurable *in vivo*. Numerous researchers have used this paradigm to explore improvements in cardiovascular diagnoses and treatments, and the biomechanical underpinnings of diseases. This paradigm has also recently gained broad clinical use for coronary artery disease diagnosis.

The vast majority of applications of image-based hemodynamics modeling have been in vascular domains. Cardiac applications, while existing, are far less common. This is despite the fact that intracardiac hemodynamics are known to be important in the initiation and progression of heart diseases, e.g., [1–7]. There are two main approaches to modeling intracardiac hemodynamics. The first approach tracks the deformation of the heart from time-resolved imaging and imposes this motion to the fluidic domains inside the heart, which leads to a deforming-domain CFD problem [8–13]. The second approach couples electro-

physiology, structural mechanics and fluid dynamics in the heart so that the heart motion is solved for rather than measured [14–16]. This second approach is formidable and is generally unnecessary if the purpose of the model is to derive intracardiac hemodynamics. Therefore, a deforming-domain CFD approach is considered the *de facto* method to derive patient-specific modeling of LV hemodynamics; it is, however, not without its challenges. Namely, in comparison to most vascular applications, cardiac structures undergo large deformations, and individual cardiac structures can be difficult to differentiate from each other and the surrounding tissue. This makes generating CFD-ready cardiac models from medical image data a substantial challenge and this is regarded as the largest bottleneck in image-based CFD modeling of cardiac hemodynamics [17].

Model construction in most prior CFD studies of intracardiac hemodynamics has required significant human effort [8–12, 17, 18]. A typical model construction workflow starts with the delineation of endocardial surfaces by manual or semi-automated image-segmentation. Most studies target left ventricle (LV) hemodynamics, and thus segment the LV, and often portions of the left atrium (LA) and aorta (Ao) inflow and outflow tracks. This is done for a sequence of image snapshots of the heart throughout the cardiac cycle, resulting in a sequence of segmentations over time. The segmented regions from a chosen time instant are used to generate a reference volumetric mesh of the fluidic domain using appropriate mesh generation software. Then a registration process is performed to deform this reference volumetric mesh so that its boundary is consistent with the image segmentation sequence. These steps are generally performed using separate software tools, which further complicates the workflow and data management. And the manual nature of the process is prone to operator-dependent errors that are unpredictable, complicating reliability and reproducibility.

Some recent works have sought to accelerate part of the model construction process. Schenkel, et al. [19] accelerated LV segmentation by fitting LV contours that depended on manual seed placements and manual segmentation of the valve ring. Nguyen, et al. [20] presented a semi-automatic, minimal operator involvement approach for LV meshing, smoothing and reconstruction but used simplified LV geometries generated from a closed-source software. Khalafvand, et al. [21] developed a semi-automatic pipeline using automated multi-atlas segmentation and statistic shape modeling of the LV, but only studied the effect of shape changes on LV flow and did not apply the method to patient-specific image data. Vellguth, et al. [22] developed an efficient pipeline using semi-automatic segmentation and geometric modeling packages but applied the pipelines to only one set of patient data. These recent approaches, while accelerating some part of the model construction process, still require various operator-dependent steps, employ closed-source

software packages, or have been tested with very few examples. A need remains to develop an automated method to reliably generate patient-specific LV CFD models directly from image data.

Following recent developments in deep learning, automated segmentation of cardiac structures using convolutional neural networks (CNNs) has gained momentum. Indeed, several deep-learning-based approaches have achieved higher segmentation precision than the previous model- or atlas-based segmentation approaches [23–26]. However, prior works in this area have been focused on the classification of cardiac structures and, to our knowledge, none have considered the construction of models suitable for computational modeling. Namely, since most deep learning approaches focus on voxel-based classification, e.g., without consideration of the overall topology of segmented structures, the utility of automatic CNN-based segmentation for computational modeling remains unclear.

Building on prior work in the area of learning-based image classification, we present here an automated framework to generate CFD-ready models from cardiac CT or MR scans. Our framework proposes a CNN-based method to perform automatic segmentation of cardiac tissues from clinical imaging. We demonstrate that our method outperforms several recently-published grand-challenge segmentation algorithms [24]. We further develop automated surface processing and image registration to generate deforming volumetric computational models suitable for deforming mesh CFD simulations. The proposed framework can be executed from the command-line (i.e., requires no visual interventions from the user) as an automated process and has only open-source software dependencies. We validate our model construction using both CT and MR benchmark image data sets, and we demonstrate the viability of using the models to perform CFD simulations of intraventricular hemodynamics.

METHODS

The proposed automated framework consists of three major steps to generate CFD-compatible models for LV flow simulations: segmentation, mesh generation and registration. For reference, the proposed process is over-viewed in Figure 1.

Patient Image Data

The MMWHS dataset was recently established as part of a grand challenge to evaluate different algorithms of whole heart segmentation [24]. The CT images were obtained from routine cardiac CT angiography and the MR images were acquired by using 3D b-SSFP sequences. The mean axial in-plane resolution for CT was 0.78 x 0.78 mm and the average slice thickness was 1.6 mm. The image resolution for the MR

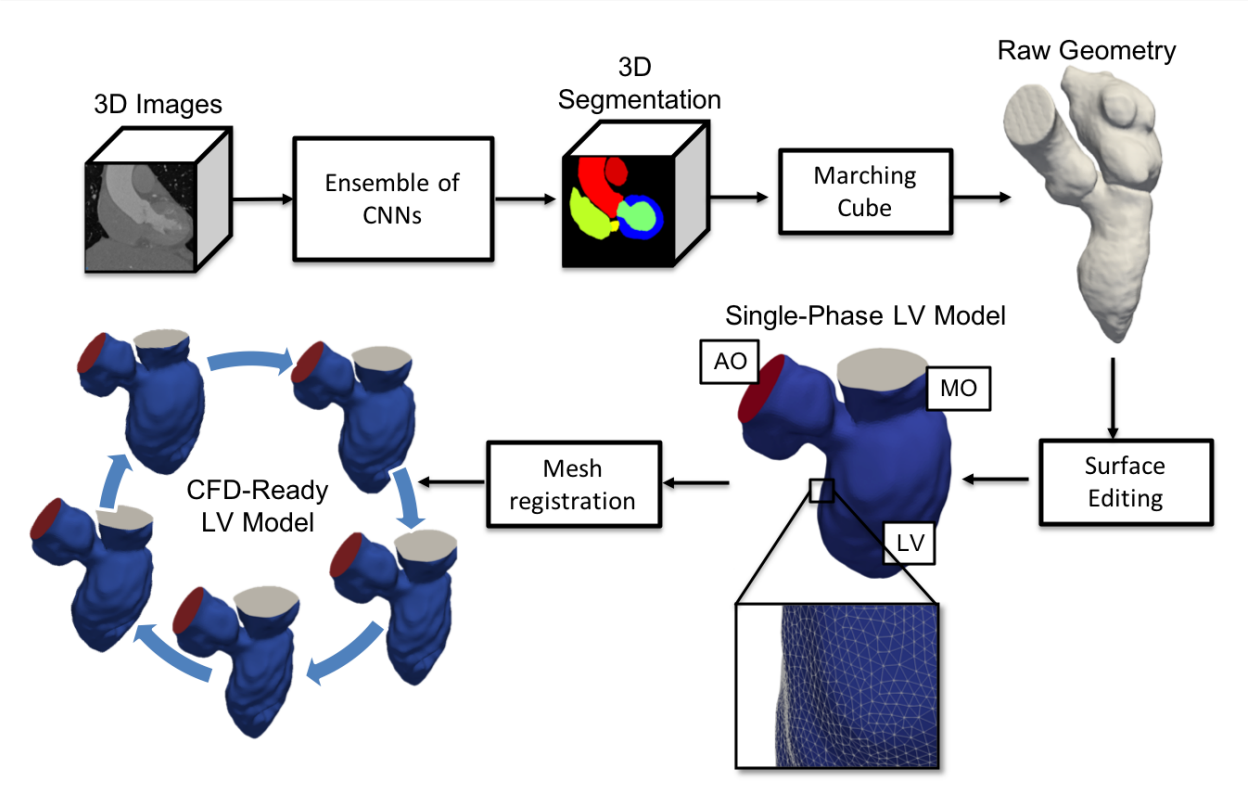

Fig. 1. Diagram of the automated model generation framework for LV CFD simulations

data was re-sampled to around 2 mm along each direction. The imaging window generally spanned from the upper abdomen to the aortic arch. The patients imaged by MR had a variety of cardiovascular diseases, including myocardium infarction, atrial fibrillation, tricuspid regurgitation, aortic valve stenosis, Alagille syndrome, Williams syndrome, dilated cardiomyopathy, aortic coarctation, and Tetralogy of Fallot [24]. The dataset includes 60 CT and 60 MR scans. 20 CT and 20 MR scans were released as training data, which contained manual segmentation of seven cardiac structures: LV, LA, RA, RV, myocardium, aorta and pulmonary artery. The remaining 40 CT and 40 MR scans were considered test data, with no provided manual segmentation as ground truth. Some datasets included segmentation of the coronary arteries and/or LA appendage, but these were not considered for the analyses herein.

Image-based CFD simulation of LV hemodynamics requires cardiac motion over one or more cardiac cycles. The MMWHS dataset only contains CT or MR scans of a single time frame. This is sufficient for testing the accuracy of our automated segmentation process, which is expected to be the most critical step in developing accurate models. However, to test the registration process (and ultimately run CFD simulations) time-resolved image data is required. For this purpose, time-resolved CT data sets were used

to verify the complete framework. The time-resolved CT data came from a 74-year-old male patient and a 73-year-old male patient, respectively. Both patients had left ventricular diastolic dysfunction. The data was de-identified and previously collected for other purposes. The mean axial in-plane resolution was 0.44 x 0.44 mm and the slice thickness was 1.25 mm. The temporal resolution was around 100 ms and 10 time frames were constructed for one cardiac cycle.

Intensity normalization and re-sampling were applied to all 3D image volumes to obtain consistent image dimensions, pixel spacing and pixel intensity range. The pre-processed image volumes can then serve as inputs to an automatic segmentation framework to generate segmentations. We first normalized pixel intensity values of each image volume such that they ranged from -1 to 1. Namely, CT intensity values, nominally ranging from around -1000 to 3000, were clipped to intensity values from -750 to 750. The cardiac tissues are well within this range while the intensity variations from bones or background noise could be mostly removed. The intensity values were then divided by 750 such that they ranged from -1 to 1. For MR, the intensity values depend not only on tissue properties but also on the MR signal intensity in individual patient scans. Therefore, for each patient MR scan, the pixels intensity values were clipped between 0 and the 99th percentile to reduce bright artifacts. The pixel values were then normalized by the maximum intensity after clipping and then shifted such that they ranged from -1 to 1. The 3D image volumes were resampled to have isotropic spacing and resized to $256 \times 256 \times 256$, which maintained image resolution with a manageable computational cost.

Automated Segmentation

Automatic Segmentation Using an Ensemble of CNNs

Our framework employed an ensemble of CNN models as described here. Broadly, using the images as inputs, a CNN-based model outputs the probability of each image pixel belonging to a particular anatomical domain (LV, LA, RA, RV, myocardium, aorta and pulmonary artery). Limited by their high memory consumption and computational cost, CNN-based 3D segmentation algorithms usually require down-sampling the input data or adopting a sliding-window strategy to avoid running out of memory. Such compromises may lead to either low spatial resolution of the segmentation results or high time complexity, respectively. Since 2D CNN-based algorithms can be directly end-to-end trained, it is possible to slice 3D image data into a number of 2D slices and then use a 2D-based algorithm on each slice. However, 2D CNN-based algorithms ignore the spatial connection between adjacent slices and thus are not able to fully explore inter-slice information as compared to 3D CNNs. Therefore, to overcome the memory constraint of performing

a 3D CNN, and information loss of performing 2D CNNs, we utilized an ensemble of 2D CNNs to generate a 3D segmentation (Figure 2a). Since deep neural network models generally have high prediction variance, ensemble learning with deep neural networks can reduce the variance and thus better generalize to unseen data [27, 28]. We sliced the 3D image volumes along the axial, sagittal or coronal axis to obtain corresponding 2D image datasets. A CNN model was trained for each 2D dataset to predict the probability of each pixel belonging to each cardiac structure. To automatically segment a new 3D image volume, we sliced the image volume into 2D images along the axial, coronal and sagittal axes, respectively, and utilized the corresponding trained 2D CNN model to predict the 2D probability maps of the sliced images in each viewing axis. The 2D predictions for slices along the same viewing axis were stacked together to form 3D predictions. These three 3D predictions, each derived from a different viewing axes, were then averaged to obtain the final probability prediction. The determination of each 3D anatomical domain was then achieved by finding the regions with the largest probability for each pixel. This automatic segmentation process is summarized in Algorithm 1.

Algorithm 1: Automatic Segmentation Using an Ensemble of CNNs

Input 3D CT/MR image I; 2D CNNs trained separately for three views
Output 3D segmentation S
Initialize a 3D probability volume P with zeros
for *each view* i **do**
  for *each 2D slice* s *in view* i **do**
    Compute the 2D probability map with the 2D CNN trained for view i
  end
  Assemble 2D probability maps into a 3D probability volume P_i
  $P \leftarrow P + P_i$
end
$P \leftarrow P/3$; `// Compute average probability map`
for *each voxel* k *in* S **do**
  $S(k) \leftarrow$ segmentation domain with the highest probability value in $P(k)$
end

Network Architecture

The 2D CNN models were implemented based on the U-Net architecture specialized for medical image segmentation [29] (Figure 2b). The network architecture included a down-sampling path (left side) to extract features from input images and an up-sampling path (right side) to reconstruct segmentation from extracted features. The down-sampling path included five convolution blocks. Each convolution block consisted of repeated convolutions with multiple 3×3 convolution kernels, followed by activation functions and 2×2

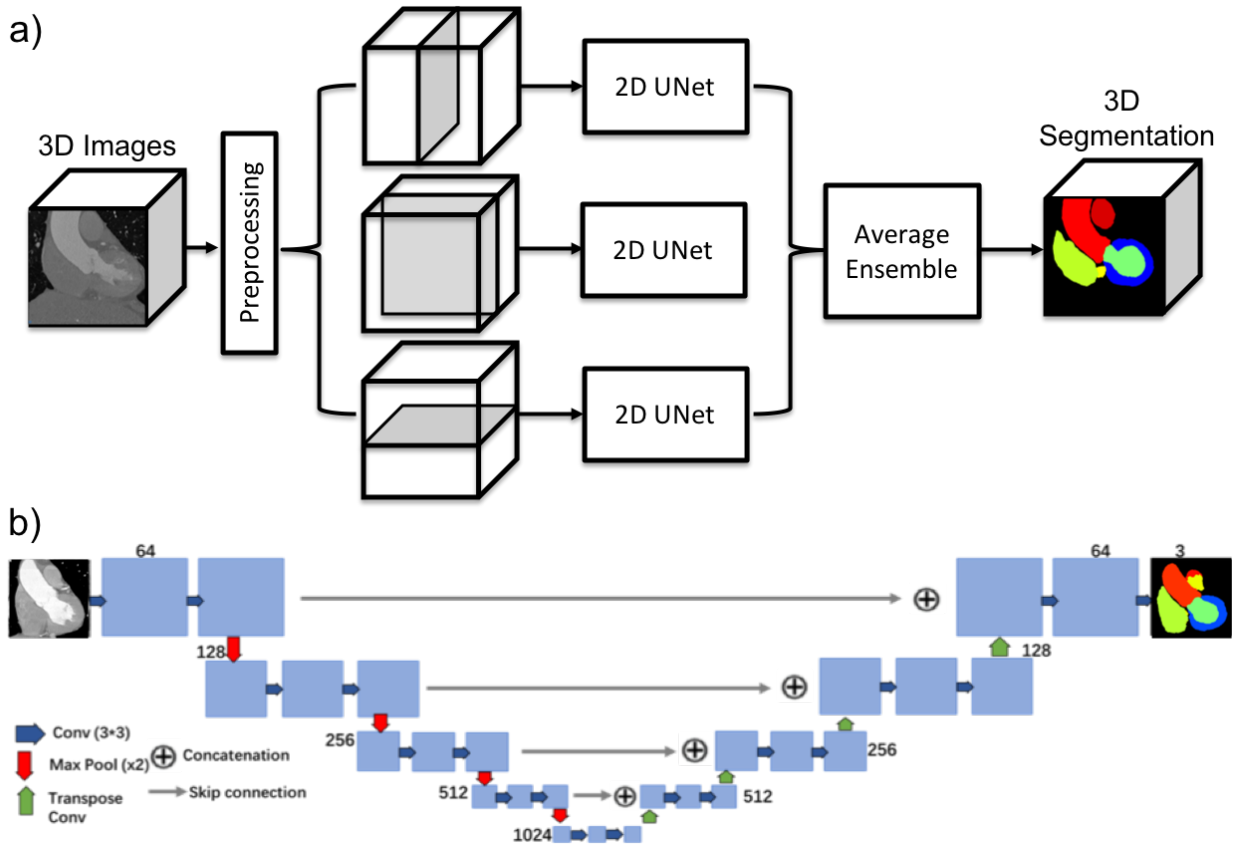

Fig. 2. a) Diagram of the proposed automatic segmentation approach using an ensemble of CNNs. b) Network architecture of the 2D U-Net CNN model. Numbers illustrate the number of convolution kernels used.

max pooling operations. The activation function was the rectified linear unit (ReLU), $f(x) = \max(0, x)$. The max-pooling operation selected the maximum value within a 2×2 window applied across the activation output and thus halved the spatial-resolution of the output. The up-sampling path included four convolution blocks and each block consisted of a transpose convolution and repeated convolutions with multiple 3×3 convolution kernels, followed by ReLU activation functions. The transpose convolutions utilized 2×2 kernels with trainable weights to recover the spatial dimension of the intermediate output. An additional convolution layer was applied at the end to generate an 8-channel probability map, with each channel corresponding to each cardiac domain. Skip connections concatenated the intermediate output from each convolution block of the down-sampling path to the corresponding convolution block input of the up-sampling path.

CNN Optimization

The training of our CNN models was supervised by the manual ground truth segmentation in the MMWHS dataset. We considered a hybrid loss function that contained both multi-class cross-entropy and

dice-score loss. Namely, let $L(I, G)$ denote the loss of between the CNN prediction P for image I and the corresponding one-hot coded ground truth segmentation G. The hybrid loss function was

$$L(I,G) = -\frac{1}{N}\sum_{i=1}^{N}\sum_{x\in I} G_i(x)\log(P_i(x)) + N - \sum_{i=1}^{N}\frac{2\sum_{x\in I} G_i(x)P_i(x)}{\sum_{x\in I} G_i(x) + \sum_{x\in I} P_i(x)} \quad (1)$$

where N denotes the total number of the segmentation (anatomical) domains, while x denotes the pixel in the input image I. $P_i(x)$ represents the predicted probability of pixel x belonging to the segmentation domain i. Weights of the convolution kernels we computed by minimizing the above loss function using the Adam stochastic gradient descent algorithm [30]. The initial learning rate was set to be 0.0001, while β_1 and β_2 for the Adam algorithm were set to 0.9 and 0.999, respectively. Among the 20 CT and 20 MR patient scans, 16 CT and 16 MR scans were randomly chosen as training data. The other CT and MR scans were considered as validation data to select the best-performing model. Dice score was evaluated on the validation data after each training epoch and the CNN model was saved after one epoch only if the validation dice score had improved. Therefore, only the CNN model with the best validation dice score was chosen for future evaluation on the held-out test dataset (which contained another set of 40 CT and 40 MR scans). We adopted a learning rate schedule where the learning rate was reduced by 20% if the validation dice score had not improved for 5 epochs. The minimum learning rate was 5×10^{-6}. The CNN models were trained on a GeForce GTX 1080 Ti GPU until the validation dice score converged. Data augmentation techniques of random flipping, random shifting, random scaling and random intensity changes were also applied during training to improve robustness. This automated segmentation algorithm was implemented using the functionality of TensorFlow (version 1.12) [31].

Evaluation Metrics And Statistical Methods

Segmentation accuracy was evaluated with an executable provided by MMWHS organizers [24], which computed the surface-to-surface distance errors as well as dice and jaccard scores between our segmentation results and the (hidden) ground truth as determined by the MMWHS organizers. Dice and jaccard scores are similarity indices that range from 0 to 1 as given by

$$\text{Dice}(A,B) = \frac{2|A\cap B|}{|A|+|B|} \quad (2)$$

$$\text{Jaccard}(A, B) = \frac{|A \cap B|}{|A \cup B|} \tag{3}$$

Differences in segmentation accuracy among segmentation domains were quantified using paired *t*-tests.

Geometry Reconstruction and Mesh Generation

We automated the geometry reconstruction and mesh generation process as described here. The entire process was implemented in Python with open-source, Python scriptable dependencies, VTK and SimVascular. For each segmentation region (LV, LA, Ao), the largest connected region of each segmentation domain was extracted to remove any disconnected islands. These segmentations were then smoothed by a closing filter that filled any sharp corners and holes with a diameter smaller than 5 mm to correct non-physical segmentation artifacts. Conversely, an opening filter was applied to remove any extrusions with diameters smaller than 5 mm. Boundaries of the Ao and LA were identified. Since the ground truth segmentation results did not consider the tissue thickness of the LA or Ao, LA and Ao segmentations were sometimes connected, leading to an incorrect fusion between the constructed LA and Ao surfaces. Therefore, LA and Ao segmentations at the location of any shared boundary were eroded until they were distinctly separated. The segmentation volume containing LA, Ao and LV segmentations was then converted to a binary segmentation volume and re-sampled with a resolution of $1.2 \times 1.2 \times 1.2$ mm. Illustrations of the above segmentation processing is shown in Figure 3.

A marching cube algorithm was applied to the processed segmentations to generate a watertight surface mesh of the LV, LA and aorta. In order to define appropriate inlet and outlet surfaces, clipping of the Ao and LA is generally necessary. To achieve this, the boundary between the LV and LA (LV and Ao) was identified as the set of points shared between the respective segmentations. The mitral plane (aortic plane) was fitted through those points. The mitral plane origin (aortic plane origin) was defined by the centroid. The LA was clipped by defining a clipping plane parallel to, and 22 mm from, the mitral plane. The aorta was clipped using a plane parallel to, and 45 mm from, the aortic plane origin. Based on our observations, these distance were large enough to avoid substantial boundary effects but small enough to avoid the computational model from being unnecessarily large. We note that naive trimming would generally truncate other parts of the model than intended. We, therefore, constructed trimmers that isolated, respectively, the LA or Ao regions, trimmed these isolated regions, and mapped the results back to the unified model. The resulting mitral opening (MO) and aortic opening (AO) were smoothed by projecting the mesh vertices to their fitted plane and applying Laplacian smoothing on nearby mesh elements. The obtained MO and AO

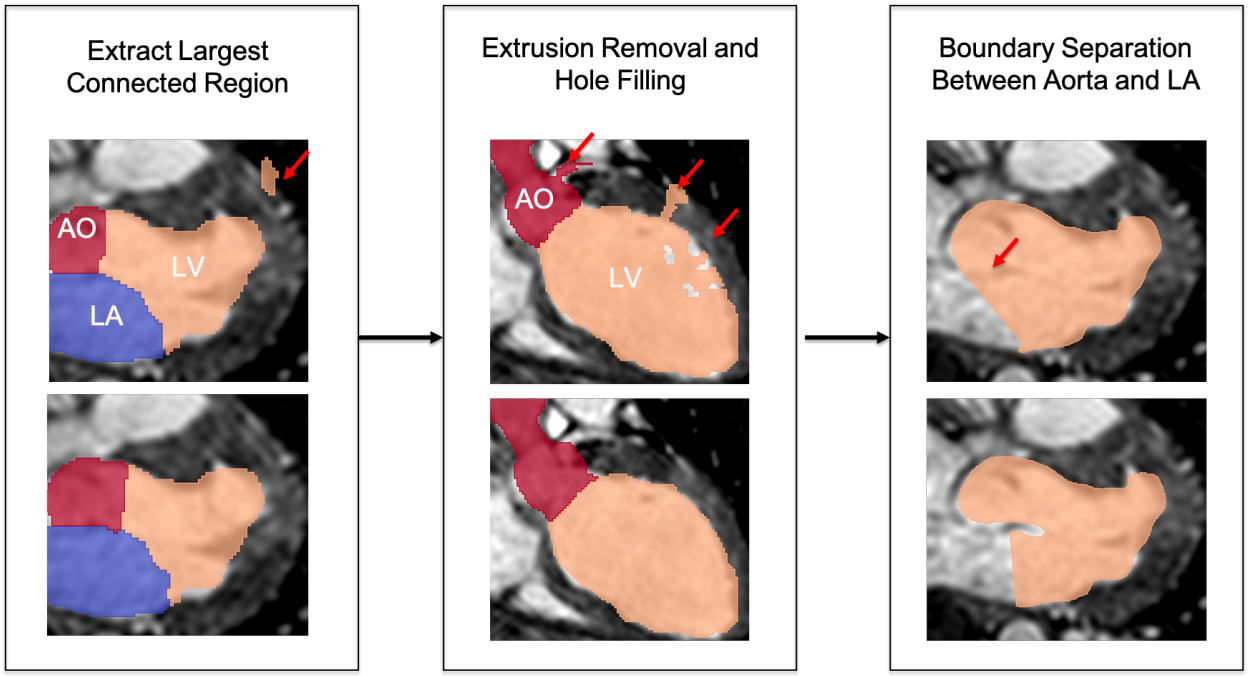

Fig. 3. Illustrations of segmentation errors corrected by segmentation processing. Top and bottom images display segmentation results before and after described segmentation processing. Red arrows indicate locations of artifacts that segmentation processing corrects. Orange, red and blue shadings on the left and middle panels represent respectively, LV, AO and LA segmentations. The orange shading on the right panel shows the processed binary segmentation of LV with parts of AO and LA combined.

were then triangulated using a constrained 2D Delaunay algorithm.

SimVascular meshing functionality [32], utilizing a combination of custom code, MMG, VMTK and TetGen, was used to generate high-quality surface and volume meshes. First, the trimmed model is remeshed with a maximum mesh edge size of 1.0 mm. Second, a volume mesh is generated with a maximum mesh edge size of 1.5 mm and a boundary layer meshing near walls. Third, non-rigid image registration of the segmentations was performed automatically (by python scripting of SimpleElastix [33]), to appropriately deform the volume mesh over time. During this process, points located on the MO or AO were projected to their least-square fit plane to ensure that they remained co-planar. The mesh generation process is shown schematically in Figure 4.

Image-Based LV CFD Simulations

We applied the Arbitrary Lagrangian-Eulerian (ALE) formulation of the incompressible Navier-Stokes equations to simulate the intraventricular flow and account for deforming volumetric mesh. The weak formulation of the Navier-Stokes equations defined in ALE coordinates for the 3D moving domain $\Omega(t) \in \mathbb{R}^3$ is given as follows:

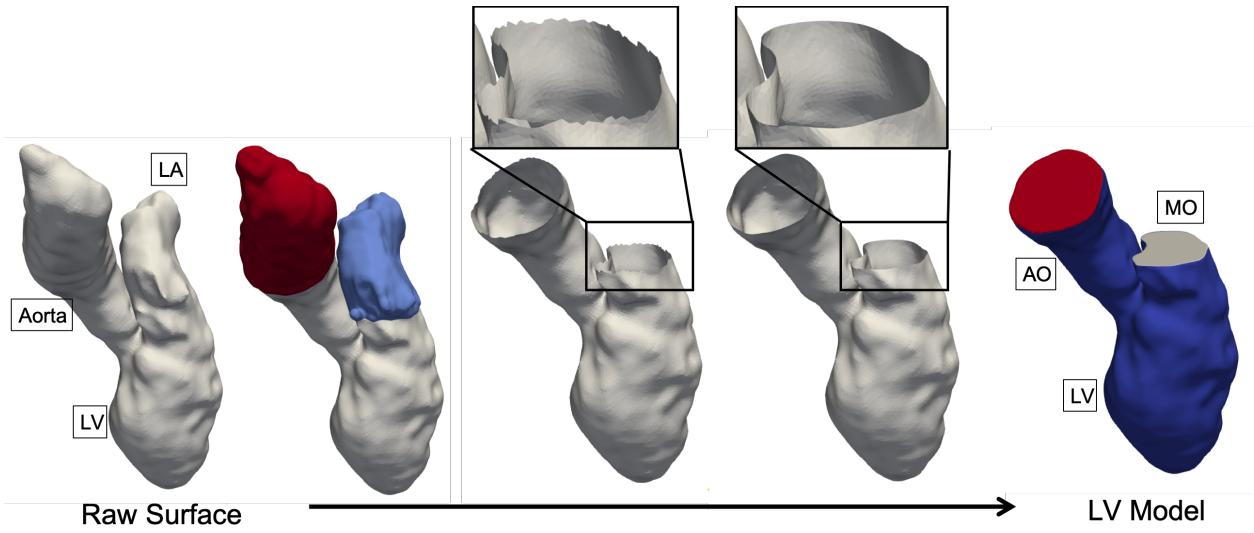

Fig. 4. Surface processing strategies for converting raw surfaces processed by the marching cube algorithm to CFD-suitable LV meshes. From left to right showing a raw surface generated by the marching cube algorithm, the raw surface with its aorta (red) and LA (light blue) trimmers, the trimmed LV model with parts of aorta and LA, the LV model with smoothed aortic and mitral openings, and the completed LV model with identified boundary faces of LV wall, mitral opening (MO) and aortic opening (AO) in dark blue, gray and red.

Find fluid velocity $\mathbf{v} \in \mathcal{S}_v$ and pressure $p \in \mathcal{S}_p$, such that for all test functions $\mathbf{w} \in \mathcal{V}_v$ and $q \in \mathcal{V}_p$,

$$B(\{\mathbf{w}, q\}, \{\mathbf{v}, p\}, \hat{\mathbf{v}}) = F(\mathbf{w}) \quad \text{where,} \tag{4a}$$

$$\begin{aligned} B(\{\mathbf{w}, q\}, \{\mathbf{v}, p\}, \hat{\mathbf{v}}) = &\langle \mathbf{w}, \rho\left(\dot{\mathbf{v}} + (\mathbf{v} - \hat{\mathbf{v}}) \cdot \nabla \mathbf{v}\right)\rangle_{\Omega(t)} \\ &- \langle \nabla \cdot \mathbf{w}, p\rangle + \langle \nabla^s \mathbf{w}, 2\mu \nabla^s \mathbf{v}\rangle_{\Omega(t)} + \langle q, \nabla \cdot \mathbf{v}\rangle_{\Omega(t)} \end{aligned} \tag{4b}$$

$$F(\mathbf{w}) = \langle \mathbf{w}, \mathbf{h}\rangle_{\Gamma(t)} \tag{4c}$$

where $\langle ., . \rangle$ represents the integral inner product over domain $\Omega(t)$, ∇^s is the symmetrization of gradient operator ∇, $\hat{\mathbf{v}}$ represents the mesh velocity defined as $\hat{\mathbf{v}} = \frac{\mathbf{x_{t+1}} - \mathbf{x_t}}{\Delta t}$. $\mathbf{h}$ represents boundary traction. Blood was assumed to have a viscosity μ of $4.0 \times 10^{-3} Pa \cdot s$ and a density ρ of $1.06 g/cm^3$. The equations were solved with the open-source svFSI solver from the SimVascular project [32, 34].

We note that LV surface and volume meshes were created at the end of diastole and propagated to different time frames. Since time resolution of the image data is too coarse to be used directly in time-stepping of the Navier-Stokes equations, cubic spline interpolation of the mesh motion was applied to generate 2000 interpolated meshes. The mesh motions computed from these interpolated meshes were

Table 1. Dice and jaccard scores and surface distance (SD) accuracy of our LV, LA, Ao and WH segmentations. Our WH segmentation accuracy is compared with the top-performing algorithm from the MMWHS grand challenge [24]. All accuracy measures are represented by mean $\pm$ standard deviation, which are computed over different patients.

		LV	LA	Ao	WH	WH (top) [24]
CT	Dice	0.938$\pm$0.042	0.936$\pm$0.027	0.95$\pm$0.02	0.92$\pm$0.022	0.908$\pm$0.086
	Jaccard	0.886$\pm$0.07	0.88$\pm$0.047	0.905$\pm$0.036	0.852$\pm$0.036	0.823$\pm$0.037
	SD (mm)	0.84$\pm$0.647	0.941$\pm$0.318	0.498$\pm$0.177	0.978$\pm$0.283	1.117$\pm$0.25
MR	Dice	0.915$\pm$0.051	0.871$\pm$0.064	0.869$\pm$0.083	0.871$\pm$0.05	0.874$\pm$0.039
	Jaccard	0.847$\pm$0.077	0.776$\pm$0.089	0.776$\pm$0.113	0.775$\pm$0.072	0.778$\pm$0.06
	SD (mm)	1.155$\pm$0.667	1.393$\pm$0.524	2.384$\pm$1.758	1.612$\pm$0.577	1.631$\pm$0.58

imposed as Dirichlet boundary conditions on walls, and to the MO during systole, or to the AO during diastole. Neumann (prescribed pressure) boundary conditions were applied to the mitral inlet during diastole or to the aortic inlet during systole. Diastole and systole phases were determined based on the increase and decrease of LV volume.

RESULTS

We tested segmentation accuracy on the 40 patient CT scans and 40 patient MR scans from the MMWHS test data set. These data were not used in any way to train the model. Table 1 displays the dice and jaccard scores and average surface distance errors of the LV, LA and Ao produced by our automated segmentation framework. The MMWHS grand challenge [24] reports these measures for whole-heart (WH) segmentation results (which includes all seven segmented cardiac tissue domains) from challenge participants. In Table 1 we compare our WH segmentation accuracy with the *top performing* algorithm from the grand challenge. For CT data, our WH segmentations outperformed the top-performing algorithm in all metrics–mean dice score, jaccard score and mean average surface distance error. For MR data, our WH segmentation results achieved better mean average surface distance errors than the top-performing algorithm but had slightly lower mean dice and jaccard scores.

To provide further details on segmentation accuracy, the box plots in Fig. 5 give the distributions of the segmentation accuracy measures for LV, Ao, LA and WH segmentation. For CT data, both LV and Ao segmentations were more accurate than WH segmentation in terms of dice score ($p < 0.01$) and jaccard score ($p < 0.001$). For MR data, LV segmentation was more accurate than WH segmentation across all metrics ($p < 0.001$). Altogether, our segmentation algorithm performance was comparable or better

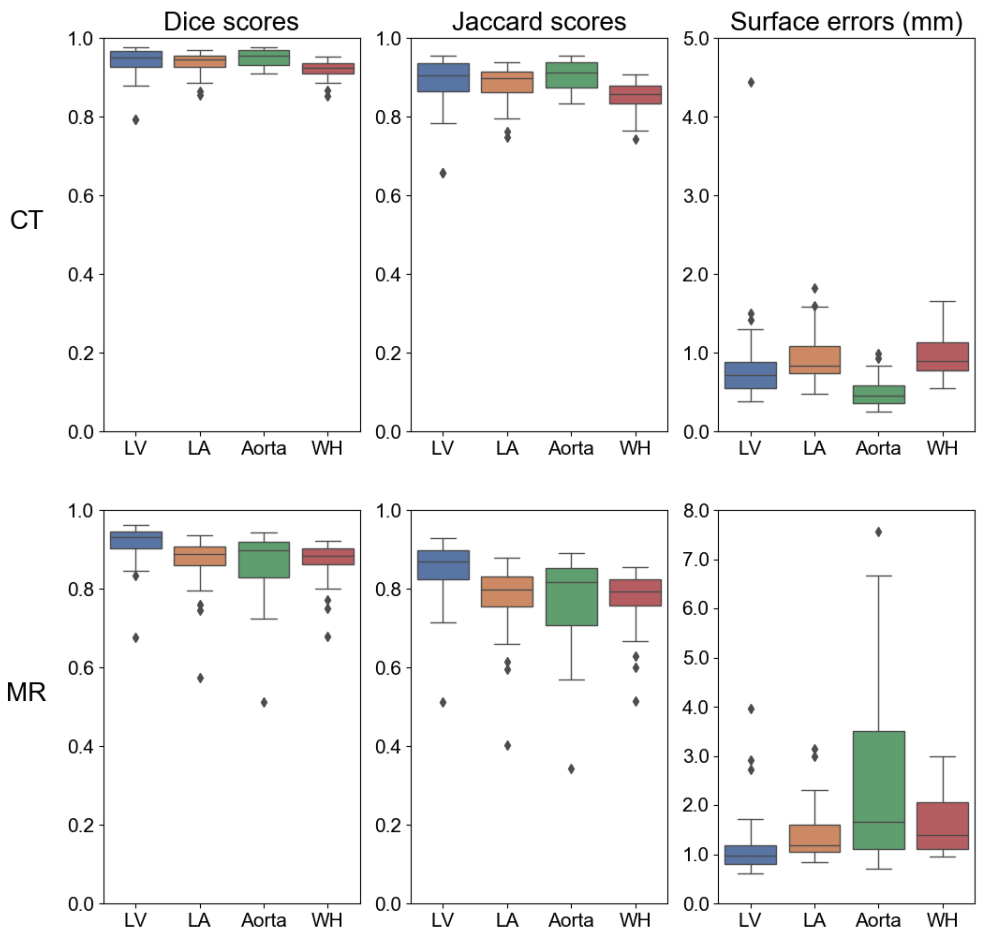

Fig. 5. Box plots of dice scores, jaccard scores and surface distance errors for LV, LA, Ao and WH segmentation results from the MMWHS test data sets.

than the most accurate grand challenge algorithms in terms of WH segmentation, and moreover, our LV segmentation, in particular, was generally more accurate than WH segmentation.

Testing the accuracy of the segmentation process is important, but only assesses the accuracy of pixel classification. This does not directly assess if segmentations will lead to valid model geometries, or domains that can be effectively meshed for CFD purposes and therefore post-processing of the segmentation results was necessary. Thus we evaluated the robustness of our geometry reconstruction and mesh generation process on the 40 CT and 40 MR scans in the MMWHS test set. We evaluated the accuracy of the

post-processed LV segmentation, whether there were any errors in geometry construction or volumetric meshing, and finally visually inspected the models for obvious artifacts. Segmentation post-processing slightly improved the LV dice score and average surface distance errors for MR data. For CT data where our segmentation framework already generated more accurate LV segmentation than MR data, post-processing slightly reduced the LV segmentation accuracy. Figure 6 displays the segmentation and the constructed LV models from the CT data within the 10th, 50th, and 90th percentiles and the "worst case" scenario encountered in terms of LV surface distance errors. For all but one segmentation results obtained from the 40 CT patient scans, our framework was able to generate the reconstructed LV geometry with LA and Ao extensions and produce a valid volumetric mesh. The remaining case had segmentation that contained holes too large to be removed by our baseline, automatic post-processing. Although model geometry and mesh were constructed, visual inspection detected large artifactual indentations. Not surprisingly this model was the one that exhibited the largest average LV surface distance error of 4.44 mm among the CT test set.

Figure 7 displays the segmentation and the corresponded LV models for MR patient data with the 10th, 50th, 90th percentiles and the "worst-case" that had the largest LV segmentation surface distance errors. Our framework was able to successfully generate CFD-suitable LV meshes automatically for 36 out of the 40 MR patient data. For 3 out of the 4 cases, we observed missing segmentation in the middle of the aorta due to poor image quality, causing the framework to be unable to identify the aortic outlet. However, this particular problem was readily corrected in practice by moving the cutting plane of aorta towards LV to reduce the length of aorta required to generate aortic outflow. Indeed, by decreasing the aortic cutting plane locations, our framework was able to succeed in these 3 cases. However, our framework was not able to generate CFD-suitable LV meshes for one remaining case without manual correction of the segmentation results. The failed case had erroneous segmentations that missed part of the cardiac structures and corresponded to the lowest WH dice scores of 0.679 and the largest mean LV surface distance errors of 3.96mm.

Figure 8 displays the distribution of model construction time, which is the time required to go from image data to a volumetrically meshed 3D model for single-phase patient CT or MR scans in the MMWHS test dataset. A 3.5 GHz Intel Core i7 CPU processor was used to evaluate geometry and mesh construction time, and a Nvidia Tesla K80 GPU was used to evaluate CNN segmentation time. The maximum, median and minimum total model generation times were 172, 126 and 102 seconds respectively for CT data and were 188, 138 and 71 seconds respectively for MR data. Model generation time for MR data was significantly longer than for CT data ($p < 0.01$) due to a longer segmentation post-processing time. On average,

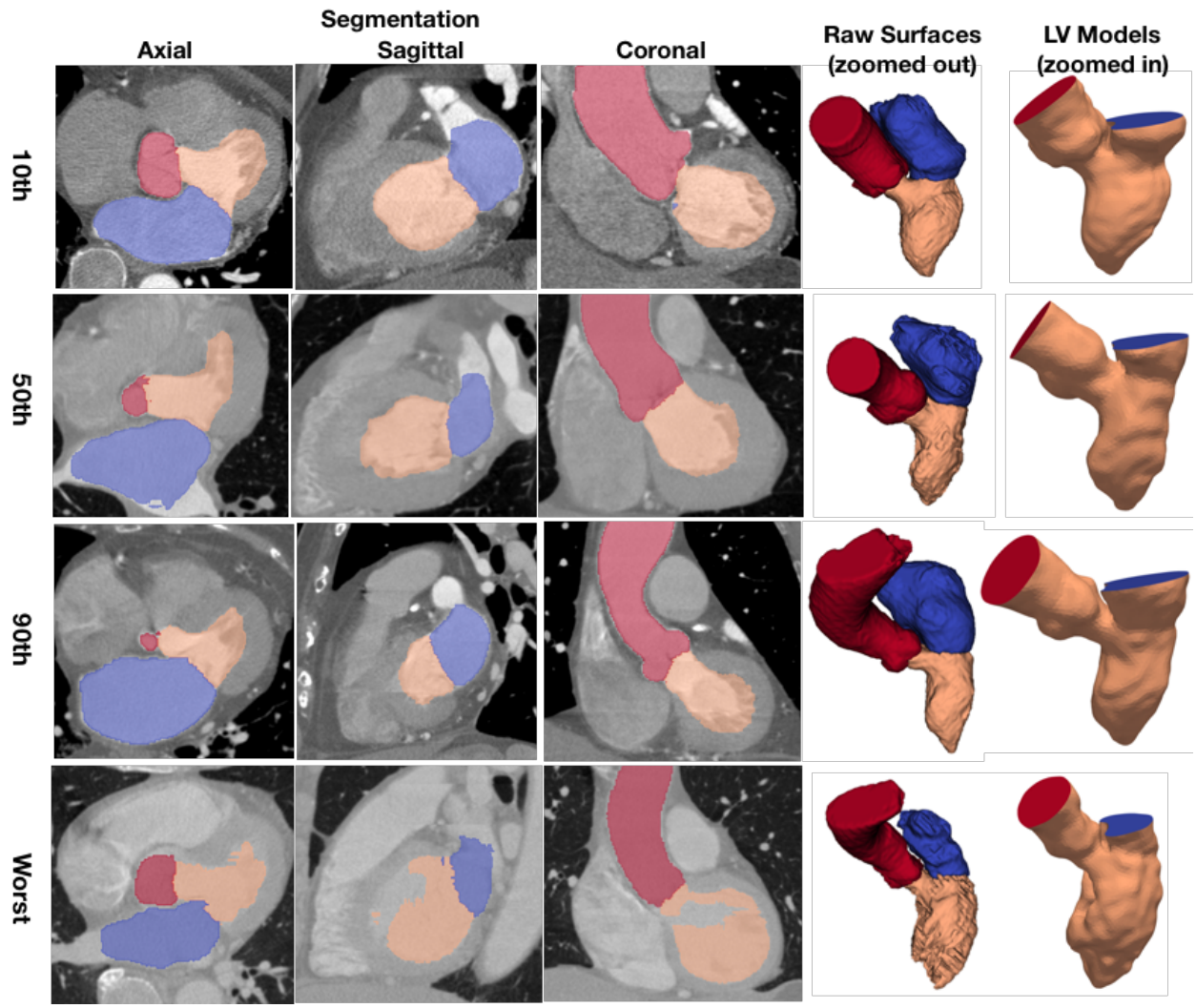

Fig. 6. Segmentation results, raw surfaces and constructed models for CT test cases with the 10th, 50th, 90th percentiles and the largest average LV segmentation surface distance errors. Segmentation and raw surfaces of LA, AO and LV are shown in blue, red and orange, respectively. The identified boundary faces of LV wall, mitral opening and aortic opening on the constructed models are shown in orange, blue and red, respectively.

the percentages of time spent in segmentation, segmentation post-processing, geometry reconstruction and meshing were 42%, 3%, 5% and 50%, respectively for CT data and were 38%, 8 %, 5 % and 49%, respectively for MR data.

CFD-ready LV models were automatically generated from the time-series CT data of two patients with diastolic dysfunction, as shown in figure 9. Non-rigid image registration took an average of 160 seconds to propagate the constructed LV model to the next time frame on a 3.5 GHz Intel Core i7 CPU processor. Interpolating the registered meshes and writing the CFD-ready model to SimVascular input files took another 158 seconds on average. To evaluate the accuracy of the reconstructed LV geometries on these

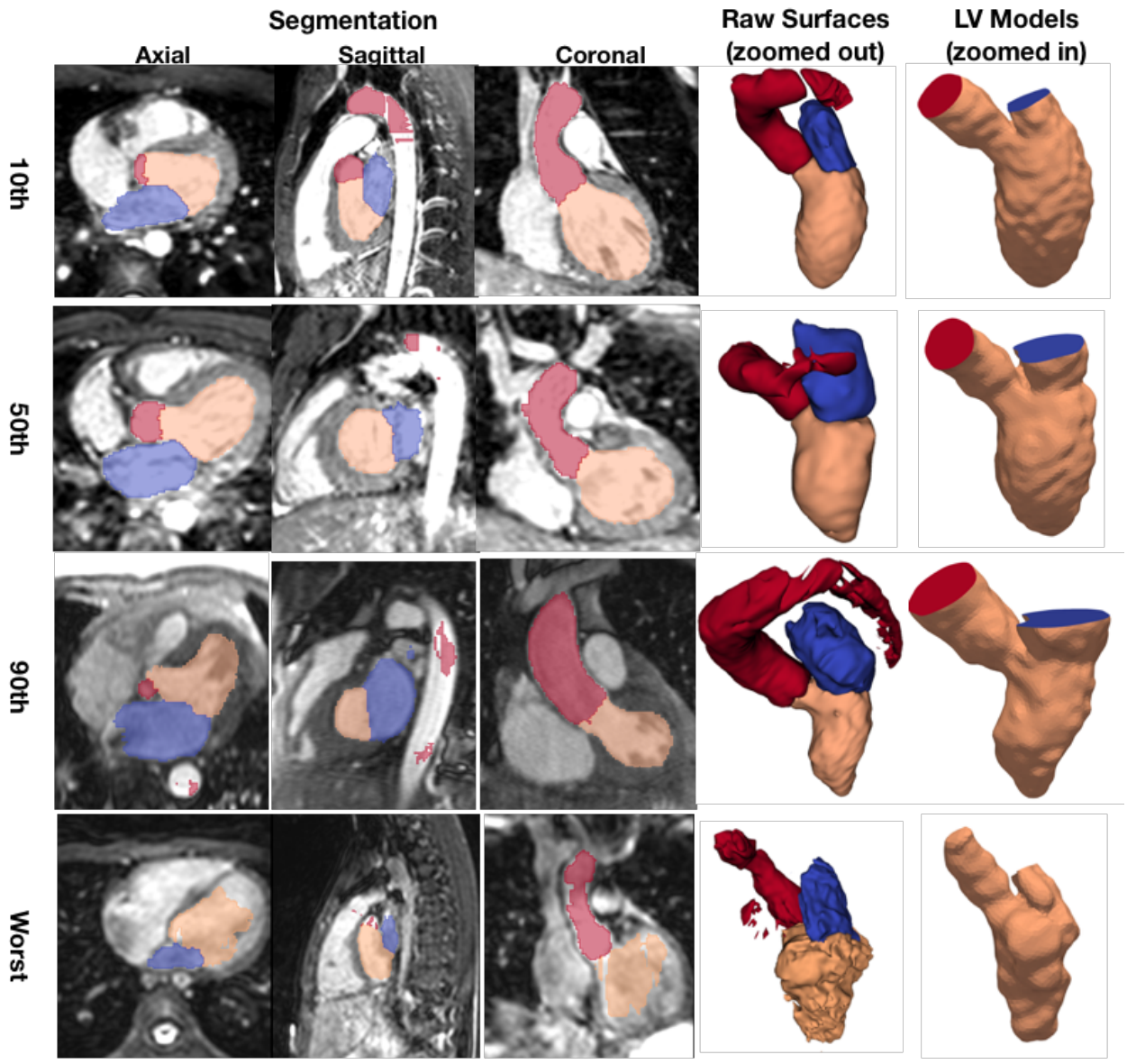

Fig. 7. Segmentation results, raw surfaces and constructed models for MR test cases with the 10th, 50th, 90th percentiles and the largest average LV segmentation surface distance errors. Segmentation and raw surfaces of LA, AO and LV are shown in blue, red and orange, respectively. The identified boundary faces of LV wall, mitral opening and aortic opening on the constructed models are shown in orange, blue and red, respectively.

time-resolved data, we used manual and semi-automatic segmentation tools provided by the open-source software SimVascular to generate a ground-truth segmentation of each time frame. We also constructed ground truth LV models with LA and Ao extensions from the ground truth segmentation. Compared with the ground truth models, the *maximum* value of the average surface distance errors among all time frames was

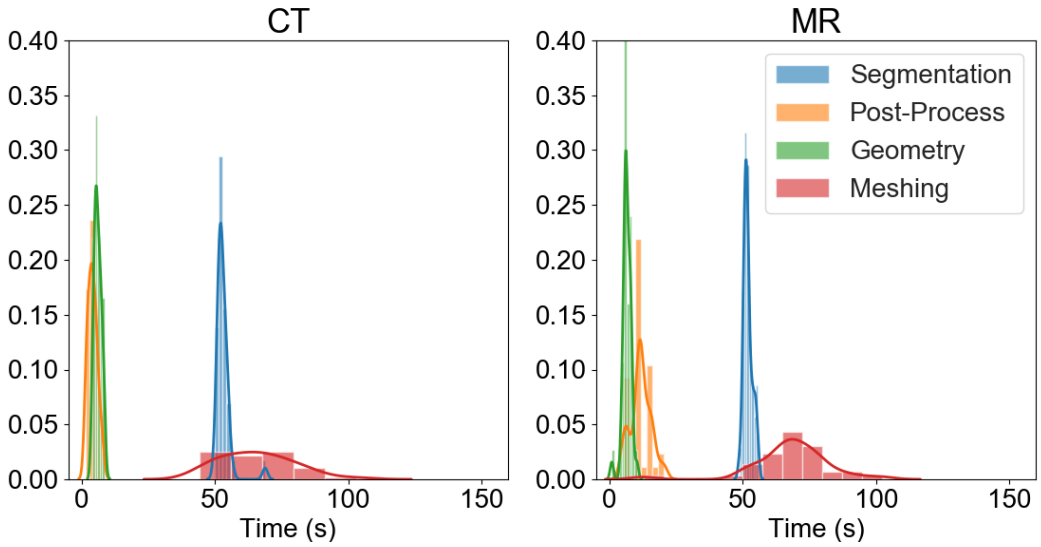

Fig. 8. Histogram distribution of the time spent in segmentation, post-processing, geometry reconstruction and meshing for CT and MR data

1.40 mm for patient A, and was 1.87 mm for patient B. Fig. 9b shows that volume curves computed from the interpolated meshes generated with our framework were similar to those computed from the ground truth for both patients and the maximum percentage differences among all time frames were 3.6% and 6.3% for patient A and B, respectively. Fig. 10 shows simulated velocity streamlines of LV flow at different time frames of the cardiac cycle. During the ejection phase, the velocity streamlines of LV demonstrated a converging flow pattern for both patients. The maximum outflow velocity during systole for patient A and patient B was 1.36 and 1.25 m/s, respectively. During diastole, we observed early filling, diastasis and atrial filling phases for both patients as shown at time C, E and F in Fig. 10. The mitral jet entered LV during early filling, changed direction due to impact with the LV wall and formed circulatory flow within the LV. During diastasis, patient A had a dominant LV vortex. With a smaller LV diameter to length ratio, patient B had a more complicated flow pattern with two major circulations, in the upper and lower parts of the LV, respectively. The maximum inflow velocity during early filling and atrial filling were 0.69 and 0.37 m/s for patient A and 0.56 and 0.28 m/s for patient B, respectively.

DISCUSSION

Imaged based CFD simulations of LV flow, although powerful in understanding patient cardiac hemodynamics, usually require significant user interactions in the model generation process. Prior studies have thus involved only a single or very few patient-based models. In the present study, we demonstrated an

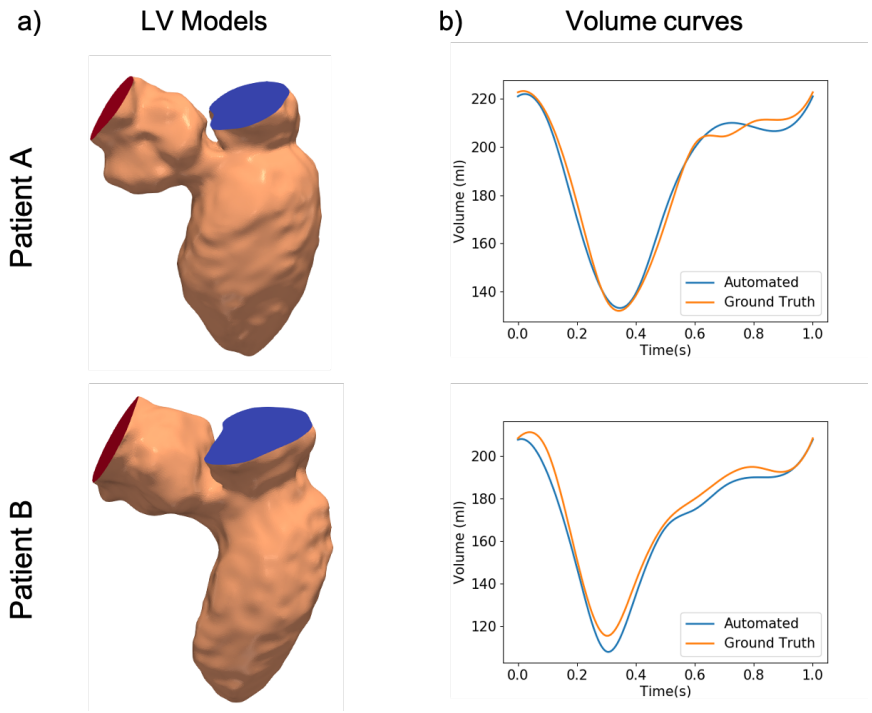

Fig. 9. Patient-specific CFD-ready LV models: a) constructed model geometries at middle diastole and b) comparisons of volume curves computed from interpolations of LV models generated with our framework (blue) and LV models generated manually (yellow) during one cardiac cycle.

automated framework to efficiently generate CFD-suitable LV models from patient data from two common imaging modalities (CT and MR) using a novel combination of deep-learning-based segmentation, geometric processing and image registration techniques.

The automated segmentation framework based on an ensemble of CNNs demonstrated promising accuracy for both CT and MR scans. Testing on the same benchmark CT data set, our framework outperformed the previous best algorithm by Payer et al. who used a two-stage 3D CNN pipeline [24, 35]. Besides increased accuracy, another advantage of our segmentation pipeline was the increased resolution of segmentation results (33% along each dimension). By using three 2D CNNs rather than 3D CNNs, our segmentation pipeline reduced the computation and memory requirements during training and thus was able to handle a larger input image size of $256 \times 256 \times 256$. A higher segmentation resolution is beneficial to the down-stream model generation process for CFD simulations since it helps to avoid the staircase artifacts due to poor image resolutions, which can affect computed hemodynamics. Moreover, most prior deep-learning-based automatic segmentation algorithms for cardiac structures have been trained on single imaging modality, except for Tong et al. who trained on both MR and CT data but did not achieve very good performance [24, 36]. We demonstrated that it is feasible to train a single system of CNN models on

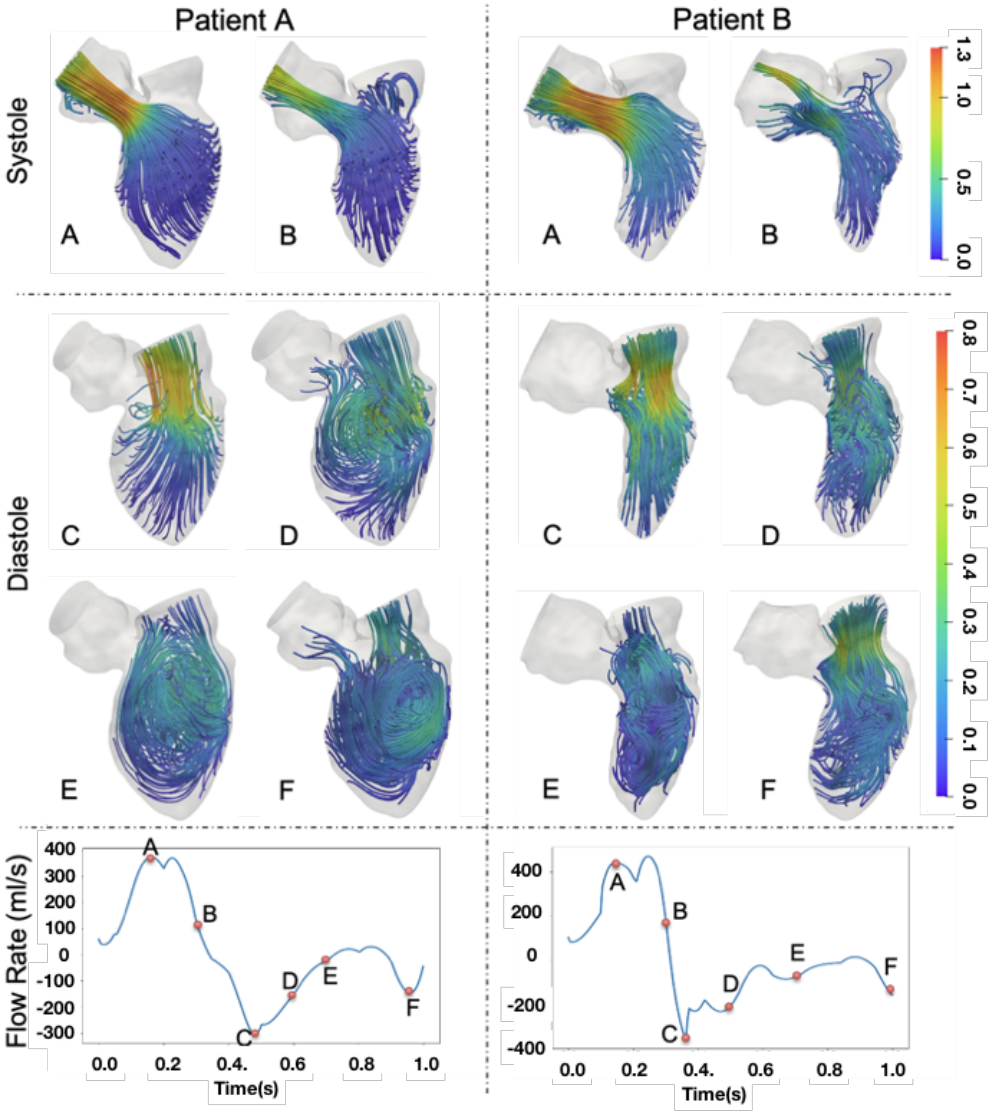

Fig. 10. Patient-specific CFD simulation results from time-resolved patient CT data. Top and middle panels show velocity streamlines at five different time frames, peak systole (A), late systole (B), early diastolic filling (C), diastasis (D) and atrial filling (E), as labeled on the flow rate curves on the bottom panel. The color map represents velocity magnitude (m/s).

MR and CT data simultaneously while still achieving good performance for both modalities. This could be explained by the high capacity of CNNs due to the large number of parameters they possess [37]. With this advantage, our framework did not require manual specification of which imaging modality to operate on and may store only one set of CNN model parameters for both MR and CT data. Compared with CT data, MR data presented larger intensity variation, acquisition field of view, image quality and uncertainties in ground truth segmentation [24]. Consistent with prior segmentation algorithms, our framework performed better in segmentation for CT data than for MR data [24]. More training data of MR scans may be required for the

deep neural networks to better capture the inherently more diverse distribution of MR data.

Although deep-learning-based algorithms have been extensively applied to LV segmentation, to our knowledge, our framework was the first to explore the down-stream geometry reconstruction procedures required to generate CFD-suitable models. Maher et al. constructed vascular models for CFD simulations from segmentation generated by deep-learning algorithms [38]; however, LV models have different geometric considerations than those of vascular models. In contrast to atlas-based segmentation approaches that attempt to map an existing atlas to new images, deep-learning-based segmentation algorithms are usually trained to optimize the voxel-wise segmentation accuracy between predicted segmentation and the ground truth, thus have no constraints on the shapes of the segmented structures. The lack of shape constraints encourages better generalization to the new and diverse data and avoids the tremendous computational cost related to atlas registration [39]; however, it poses challenges to the down-stream LV geometry reconstruction process required for generating a CFD-suitable geometry since the segmentation results are not guaranteed to have valid global topology. Indeed, it is possible to have good segmentation accuracy based on conventional ”closeness metrics” but not have a segmentation suitable for CFD model construction. In this study, we demonstrated that with a reliable deep-learning-based segmentation framework, along with simple and automatic post-processing techniques, we were able to successfully construct LV CFD models for the vast majority of cases considered. Specifically, from the segmentation results of LV, LA and aorta, small and isolated regions needed to be removed by extracting the largest connected region; boundaries between LA and aorta needed to be clearly separated to generate anatomically correct LA and aorta geometries with the marching cube algorithms; noisy extrusions or holes within and on the boundary of segmentation needed to be removed or filled. These operations were conveniently achieved by a combination of image foreground dilation or erosion functions and were successful on 39 out of 40 tested CT image data and 39 out of 40 tested MR image data. Not surprisingly, reliable segmentation results were essential to obtain accurate LV model geometries. The failed cases were due to erroneous segmentation results with large surface distance errors, missing structures or extrusions or holes too large to be corrected by the post-processing algorithms. For the small number of failed cases, manual corrections may be required to generate acceptable LV model geometries. Since our deep-learning-based segmentation algorithm was developed based on a limited number of samples, it may not generalize to all kinds of image abnormalities, such as low image quality, artifacts or extreme tissue intensity. Indeed, it is impossible to guarantee an automated approach will always produce a valid result when image quality is not controlled.

Although this study focused on the image-to-volume-mesh process, and not the analysis of intraven-

tricular hemodynamics, we did demonstrate the capability to perform ALE-based CFD simulations of LV hemodynamics from the generated models. The fact that the time-resolved CT image data were from clinical scans and from a completely different source than the MMWHS dataset demonstrates the potential robustness of the approach. Compared with ground truth LV models created through manual efforts, LV models created by our framework had a relatively small percentage of volume difference over the cardiac cycle. We note that the ground truth models were created by only one observer with no repeats. Zhuang et al. reported that while LV was the least challenging cardiac structure to segment manually among others, the inter- and intra- observer variabilities were 6.3% and 5.8% for LV segmentation in MR data [24]. Therefore, the volume differences of the LV models generated automatically are comparable to inter- and intra- observer variabilities. Our CFD simulations provided detailed LV flow patterns throughout the cardiac cycle and the converging flow pattern during systole and the circulatory flow patterns were consistent with prior studies [11, 18]. Although both patients had diastolic LV dysfunction, their LV shapes were different especially in terms of LV sphericity. We observed a dominating flow circulation in the patient LV with higher sphericity but not in the patient LV with lower sphericity. Such difference was in agreement with Martinez-Legazpi et. al., who demonstrated that reduced LV chamber sphericity could reduce vortex contribution to the diastolic filling of LV [40].

Our framework was able to generate meshed LV model for a single phase in around two minutes on average, using a modern desktop computer with the help of a GPU. When including the time spent in segmentation registration to propagate LV model to other time frames, interpolating meshes and creating compatible input files for SimVascular svFSI solver, our framework took around 30 minutes in total to construct CFD-ready LV simulation input files for one set of time-resolved patient image data with 10 time frames. Segmentation registration was the most time-consuming step among our model construction framework. However, this step could be parallelized in the future to reduce the total model generation time [41]. In contrast, prior approaches of generating one CFD-ready LV model from images could take anywhere from 20–50 hours of work and significant human efforts [16, 17]. Using the semi-automatic segmentation techniques and geometry processing algorithms in SimVascular, we spent around 10 hours constructing each LV model on the same patient data, which we consider to be typical for an “experienced” user. Therefore, compared with prior model construction approaches using manual or semi-automatic techniques, our framework could save on the order of hours of time and human efforts.

Limitations of the current automated LV CFD model generation framework include the lack of explicit mitral valve and aortic valve structures. However, valve leaflets are generally not resolvable from clinical

scans. Therefore, patient-specific geometry reconstruction of valves is very challenging due to limited image resolution and large deformation of the valve structures. Recent advances in machine-learning-based approaches to obtain heart valve geometry based on statistical information could be applied in the future to improve our framework [42, 43]. Similar to the valve leaflet, the papillary muscles and trabeculae structures of the LV were not modeled in our framework since these are generally not resolvable from clinical imaging. Although smoothed LV geometry is a common simplification adopted by many prior studies, recent studies have demonstrated that these structures could lead to improved apical washout, enhanced viscous dissipation rate, increased intra-ventricular pressure drop and reduced the wall shear stress and thus should be incorporated for better simulation accuracy [44, 45].

With improved insights into the importance of RV dysfunction in the pathogenesis and outcomes of cardiovascular diseases over recent years, there has been a growing interest in understanding the intraventricular flow pattern in RV [46–49]. Image-based CFD simulations of RV flow may provide patient-specific, spatially and temporally well-resolved analysis of RV hemodynamics. We note that although this study focused on LV, we expect the proposed framework could be readily adapted for the automated construction of patient-specific CFD-ready RV models. Our framework was able to automatically produce segmentations of RV, RA and pulmonary arteries. From those segmentations, similar segmentation post-processing and surface reconstruction procedures could be applied to reconstruct the RV geometry with appropriate inlet and outlet structures.

CONCLUSIONS

We have developed a streamlined framework to automatically generate CFD-ready LV models from patient image data. The framework leveraged a novel combination of deep-learning-based automatic segmentation algorithms and geometry processing algorithms to robustly create CFD-suitable LV models from both CT and MR image data. We utilized an ensemble of 2D CNNs to achieve high 3D segmentation resolution and outperformed previous automatic segmentation approaches evaluated on the same dataset. To support CFD simulation of LV hemodynamics using an ALE formulation, the framework can automatically identify boundary faces of mitral and aortic opening, and LV as well as computing displacement information of the mesh vertices throughout the cardiac cycle using image registration techniques. Compared with prior manual or semi-automatic methods, our framework offers orders of magnitude savings in time and human efforts in developing image-based CFD simulation of LV flow. The entire framework was implemented in Python and can be conveniently executed from the command-line as a program with all dependencies

(TensorFlow, VTK, SimVascular and SimpleElastix) being open-source and Python-scriptable. The above advantages may enable our framework to aid in future higher throughput, large-cohort analyses of patient-specific LV hemodynamics in-relation to LV dysfunction.

ACKNOWLEDGEMENTS

This work was supported by the NSF, Award #1663747. We thank Drs. Shone Almeida, Amirhossein Arzani and Kashif Shaikh for providing the time-series CT image data. We also thank MMWHS Challenge for providing the CT and the MR datasets.

REFERENCES

[1] Pedrizzetti, G., Canna, G., Alfieri, O., and Tonti, G., 2014. "The vortex - an early predictor of cardiovascular outcome?". *Nature reviews. Cardiology,* **11**, 06.

[2] Faludi, R., Szulik, M., D'hooge, J., Herijgers, P., Rademakers, F., Pedrizzetti, G., and Voigt, J.-U., 2010. "Left ventricular flow patterns in healthy subjects and patients with prosthetic mitral valves. an". *The Journal of thoracic and cardiovascular surgery,* **139**, 04, pp. 1501–10.

[3] Martinez-Legazpi, P., Bermejo, J., Benito, Y., Yotti, R., Villar, C., González-Mansilla, A., Barrio, A., Villacorta, E., Sanchez, P., Fernández-Avilés, F., and Del Alamo, J. C., 2014. "Contribution of the diastolic vortex ring to left ventricular filling". *Journal of the American College of Cardiology,* **64**, 10, pp. 1711–21.

[4] Gharib, M., Rambod, E., Kheradvar, A., Sahn, D., and Dabiri, J., 2006. "Optimal vortex formation as an index of cardiac health". *Proceedings of the National Academy of Sciences of the United States of America,* **103**, 05, pp. 6305–8.

[5] Pedrizzetti, G., Domenichini, F., and Tonti, G., 2010. "On the left ventricular vortex reversal after mitral valve replacement". *Annals of biomedical engineering,* **38**, 03, pp. 769–73.

[6] Elbaz, M. S., van der Geest, R. J., Calkoen, E. E., de Roos, A., Lelieveldt, B. P., Roest, A. A., and Westenberg, J. J., 2016. "Assessment of viscous energy loss and the association with three-dimensional vortex ring formation in left ventricular inflow: In vivo evaluation using four-dimensional flow mri". *Magnetic Resonance in Medicine,* **77**(2), 02, pp. 794–805.

[7] Eriksson, J., Dyverfeldt, P., Engvall, J., Bolger, A., Ebbers, T., and Carlhäll, C.-J., 2011. "Quantification of presystolic blood flow organization and energetics in the human left ventricle". *American journal of physiology. Heart and circulatory physiology,* **300**, 03, pp. H2135–41.

[8] Chnafa, C., Mendez, S., and Franck, N., 2016. "Image-based simulations show important flow fluctuations in a normal left ventricle: What could be the implications?". *Annals of biomedical engineering,* **44**, 04.

[9] Caballero, A., Mao, W., Liang, L., Oshinski, J., Primiano, C., McKay, R., Kodali, S., and Sun, W., 2017. "Modeling left ventricular blood flow using smoothed particle hydrodynamics". *Cardiovascular Engineering and Technology,* **8**(4), Dec, pp. 465–479.

[10] N Doost, S., Zhong, L., Su, B., and Morsi, Y. Y., 2016. "The numerical analysis of non-newtonian blood flow in human patient-specific left ventricle". *Computer Methods and Programs in Biomedicine,* **127**, 01.

[11] Khalafvand, S. S., Ng, E., Zhong, L., and Hung, T.-K., 2012. "Fluid-dynamics modelling of the human left ventricle with dynamic mesh for normal and myocardial infarction: Preliminary study". *Computers in biology and medicine,* **42**, 07, pp. 863–70.

[12] Schenkel, T., Malvè, M., Reik, M., Markl, M., Jung, B., and Oertel, H., 2008. "Mri-based cfd analysis of flow in a human left ventricle: Methodology and application to a healthy heart". *Annals of Biomedical Engineering,* **37**, pp. 503–515.

[13] Bavo, A., Pouch, A., Degroote, J., Vierendeels, J., Gorman III, J., Gorman, R., and Segers, P., 2016. "Patient-specific cfd simulation of intraventricular haemodynamics based on 3d ultrasound imaging". *Biomedical engineering online,* **15**, 09, p. 107.

[14] Santiago, A., Zavala-Aké, M., Aguado-Sierra, J., Doste, R., Gómez González, S., Arís, R., Cajas, J., Casoni, E., and Vázquez, M., 2018. "Fully coupled fluid-electro-mechanical model of the human heart for supercomputers". *International Journal for Numerical Methods in Biomedical Engineering,* **34**, 08.

[15] Karabelas, E., Gsell, M., Augustin, C., Marx, L., Neic, A., Prassl, A., Goubergrits, L., Kuehne, T., and Plank, G., 2018. "Towards a computational framework for modeling the impact of aortic coarctations upon left ventricular load". *Frontiers in Physiology,* **9**, 05, p. 538.

[16] Augustin, C., Crozier, A., Neic, A., Prassl, A., Karabelas, E., Silva, T., Fernandes, J., Campos, F., Kuehne, T., and Plank, G., 2016. "Patient-specific modeling of left ventricular electromechanics as a driver for haemodynamic analysis". *Europace,* **18**, 08, pp. iv121–iv129.

[17] Mittal, R., Seo, J. H., Vedula, V., Choi, Y., Liu, H., Huang, H., Jain, S., Younes, L., Abraham, T., and George, R., 2015. "Computational modeling of cardiac hemodynamics: Current status and future outlook". *Journal of Computational Physics,* **305**, 11.

[18] N Doost, S., Ghista, D., Su, B., Zhong, L., and Morsi, Y. Y., 2016. "Heart blood flow simulation: A

perspective review". *BioMedical Engineering OnLine,* **15**, 12.

[19] Schenkel, T., Malve, M., Reik, M., Markl, M., Jung, B., and Oertel, H., 2009. "Mri-based cfd analysis of flow in a human left ventricle: Methodology and application to a healthy heart". *Annals of biomedical engineering,* **37**, 02, pp. 503–15.

[20] Nguyen, V.-T., Chong, J. L., Huy, N., Zhong, L., and Leo, H., 2013. "A semi-automated method for patient-specific computational flow modelling of left ventricles". *Computer methods in biomechanics and biomedical engineering,* **18**, 08.

[21] Khalafvand, S. S., Voorneveld, J., Muralidharan, A., Gijsen, F., Bosch, J. G., Walsum, T., Haak, A., Jong, N., and Kenjeres, S., 2018. "Assessment of human left ventricle flow using statistical shape modelling and computational fluid dynamics". *Journal of Biomechanics,* **74**, 04.

[22] Vellguth, K., Brüning, J., Goubergrits, L., Tautz, L., Hennemuth, A., Kertzscher, U., Degener, F., Kelm, M., Sündermann, S., and Kuehne, T., 2018. "Development of a modeling pipeline for the prediction of hemodynamic outcome after virtual mitral valve repair using image-based cfd". *International Journal of Computer Assisted Radiology and Surgery*, 07.

[23] Avendi, M. R., Kheradvar, A., and Jafarkhani, H., 2015. "A combined deep-learning and deformable-model approach to fully automatic segmentation of the left ventricle in cardiac mri". *Medical image analysis,* **30**, pp. 108–119.

[24] Zhuang, X., Li, L., Payer, C., Štern, D., Urschler, M., Heinrich, M. P., Oster, J., Wang, C., Örjan Smedby, Bian, C., Yang, X., Heng, P.-A., Mortazi, A., Bagci, U., Yang, G., Sun, C., Galisot, G., Ramel, J.-Y., Brouard, T., Tong, Q., Si, W., Liao, X., Zeng, G., Shi, Z., Zheng, G., Wang, C., MacGillivray, T., Newby, D., Rhode, K., Ourselin, S., Mohiaddin, R., Keegan, J., Firmin, D., and Yang, G., 2019. "Evaluation of algorithms for multi-modality whole heart segmentation: An open-access grand challenge". *Medical Image Analysis,* **58**, p. 101537.

[25] Bernard, O., Lalande, A., Zotti, C., Cervenansky, F., Yang, X., Heng, P., Cetin, I., Lekadir, K., Camara, O., Gonzalez Ballester, M. A., Sanroma, G., Napel, S., Petersen, S., Tziritas, G., Grinias, E., Khened, M., Kollerathu, V. A., Krishnamurthi, G., Rohé, M., Pennec, X., Sermesant, M., Isensee, F., Jäger, P., Maier-Hein, K. H., Full, P. M., Wolf, I., Engelhardt, S., Baumgartner, C. F., Koch, L. M., Wolterink, J. M., Išgum, I., Jang, Y., Hong, Y., Patravali, J., Jain, S., Humbert, O., and Jodoin, P., 2018. "Deep learning techniques for automatic mri cardiac multi-structures segmentation and diagnosis: Is the problem solved?". *IEEE Transactions on Medical Imaging,* **37**(11), Nov, pp. 2514–2525.

[26] Ngo, T., Lu, Z., and Carneiro, G., 2016. "Combining deep learning and level set for the automated

segmentation of the left ventricle of the heart from cardiac cine magnetic resonance". *Medical Image Analysis,* **35**, 05.

[27] Ju, C., Bibaut, A., and Laan, M., 2017. "The relative performance of ensemble methods with deep convolutional neural networks for image classification". *Journal of Applied Statistics,* **45**, 04.

[28] Zheng, H., Zhang, Y., Yang, L., Liang, P., Zhao, Z., Wang, C., and Chen, D. Z., 2019. "A new ensemble learning framework for 3d biomedical image segmentation". In AAAI.

[29] Ronneberger, O., Fischer, P., and Brox, T., 2015. "U-net: Convolutional networks for biomedical image segmentation". In Medical Image Computing and Computer-Assisted Intervention – MICCAI 2015, N. Navab, J. Hornegger, W. M. Wells, and A. F. Frangi, eds., Springer International Publishing, pp. 234–241.

[30] Kingma, D., and Ba, J., 2014. "Adam: A method for stochastic optimization". *International Conference on Learning Representations*, 12.

[31] Abadi, M., Barham, P., Chen, J., Chen, Z., Davis, A., Dean, J., Devin, M., Ghemawat, S., Irving, G., Isard, M., et al., 2016. "Tensorflow: A system for large-scale machine learning". In 12th {USENIX} Symposium on Operating Systems Design and Implementation ({OSDI} 16), pp. 265–283.

[32] Updegrove, A., Wilson, N., Merkow, J., Lan, H., Marsden, A., and Shadden, S., 2016. "Simvascular: An open source pipeline for cardiovascular simulation". *Annals of Biomedical Engineering,* **45**, 12.

[33] Klein, S., Staring, M., Murphy, K., Viergever, M., and Pluim, J., 2009. "Elastix: A toolbox for intensity-based medical image registration". *IEEE transactions on medical imaging,* **29**, 11, pp. 196–205.

[34] SimVascular, 2020. svfsi. `https://github.com/SimVascular/svFSI`.

[35] Payer, C., Štern, D., Bischof, H., and Urschler, M., 2018. "Multi-label whole heart segmentation using cnns and anatomical label configurations". In Statistical Atlases and Computational Models of the Heart. ACDC and MMWHS Challenges, Springer, pp. 190–198.

[36] Tong, Q., Ning, M., Si, W., Liao, X., and Qin, J., 2018. "3d deeply-supervised u-net based whole heart segmentation". In Statistical Atlases and Computational Models of the Heart. ACDC and MMWHS Challenges, Springer, pp. 224–232.

[37] Moeskops, P., Wolterink, J. M., van der Velden, B. H. M., Gilhuijs, K. G. A., Leiner, T., Viergever, M. A., and Išgum, I., 2016. "Deep learning for multi-task medical image segmentation in multiple modalities". In Medical Image Computing and Computer-Assisted Intervention – MICCAI 2016, S. Ourselin, L. Joskowicz, M. R. Sabuncu, G. Unal, and W. Wells, eds., Springer International Publishing, pp. 478–486.

[38] Maher, G., Wilson, N., and Marsden, A., 2019. "Accelerating cardiovascular model building with convolutional neural networks". *Medical & Biological Engineering & Computing,* **57**, pp. 2319–2335.

[39] Iglesias, J., and Sabuncu, M., 2014. "Multi-atlas segmentation of biomedical images: A survey". *Medical image analysis,* **24**, 12.

[40] Martinez-Legazpi, P., Bermejo, J., Benito, Y., Yotti, R., Villar, C., González-Mansilla, A., Barrio, A., Villacorta, E., Sanchez, P., Fernández-Avilés, F., and Del Alamo, J. C., 2014. "Contribution of the diastolic vortex ring to left ventricular filling". *Journal of the American College of Cardiology,* **64**, 10, pp. 1711–21.

[41] Shamonin, D., Bron, E., Lelieveldt, B., Smits, M., Klein, S., and Staring, M., 2013. "Fast parallel image registration on cpu and gpu for diagnostic classification of alzheimer's disease". *Frontiers in neuroinformatics,* **7**, 01, p. 50.

[42] Pouch, A., Vergnat, M., McGarvey, J., Ferrari, G., Jackson, B., Sehgal, C., Yushkevich, P., Gorman, R., and Gorman III, J., 2013. "Statistical assessment of normal mitral annular geometry using automated three-dimensional echocardiographic analysis". *The Annals of thoracic surgery,* **97**, 10.

[43] Liang, L., Kong, F., Martin, C., Pham, T., Wang, Q., Duncan, J., and Sun, W., 2016. "Machine learning based 3d geometry reconstruction and modeling of aortic valve deformation using 3d ct images: Machine learning based 3d aortic valve modeling". *International Journal for Numerical Methods in Biomedical Engineering,* **33**, 08, p. e02827.

[44] Sacco, F., Paun, B., Lehmkuhl, O., Iles, T. L., Iaizzo, P. A., Houzeaux, G., Vázquez, M., Butakoff, C., and Aguado-Sierra, J., 2018. "Left ventricular trabeculations decrease the wall shear stress and increase the intra-ventricular pressure drop in cfd simulations". *Frontiers in Physiology,* **9**, p. 458.

[45] Vedula, V., Seo, J. H., Lardo, A., and Mittal, R., 2015. "Effect of trabeculae and papillary muscles on the hemodynamics of the left ventricle". *Theoretical and Computational Fluid Dynamics,* **30**, 05.

[46] Pasipoularides, A. D., Shu, M., Shah, A., Womack, M. S., and Glower, D. D., 2003. "Diastolic right ventricular filling vortex in normal and volume overload states.". *American journal of physiology. Heart and circulatory physiology,* **284 4**, pp. H1064–72.

[47] Sheehan, F., and Redington, A., 2008. "The right ventricle: Anatomy, physiology and clinical imaging". *Heart (British Cardiac Society),* **94**, 12, pp. 1510–5.

[48] Noordegraaf, A., Chin, K., Haddad, F., Hassoun, P., Hemnes, A., Hopkins, S., Kawut, S., Langleben, D., Lumens, J., and Naeije, R., 2018. "Pathophysiology of the right ventricle and of the pulmonary circulation in pulmonary hypertension: an update". *European Respiratory Journal,* **53**, 12, p. 1801900.

[49] Crystal, G., and Pagel, P., 2017. "Right ventricular perfusion: Physiology and clinical implications". *Anesthesiology,* **128**, 10, p. 1.

LIST OF FIGURES

LIST OF TABLES